AE monitoring of crack evolution on UHPC deck layer of a long-span cable-stayed bridge

Developments in the Built Environment 23 (2025) 100697

Contents lists available at ScienceDirect

Developments in the Built Environment

journal homepage: www.sciencedirect.com/journal/developments-in-the-built-environment

AE monitoring of crack evolution on UHPC deck layer of a long-span cable-stayed bridge

Zihan Jiang [a,b], Zhiwen Zhu [a,*], Giuseppe Lacidogna [b,**]

[a] Department of Civil Engineering and Smart Cities, Shantou University, 243 University Road, Shantou, China
[b] Department of Structural, Geotechnical and Building Engineering, Politecnico di Torino, 24, Corso Duca degli Abruzzi, 10129, Torino, Italy

ARTICLE INFO

Keywords:
Acoustic emission
Crack evolution
UHPC deck layer
b-value
Field test

ABSTRACT

The UHPC deck layer may be susceptible to cracking during construction, raising concerns for bridge engineering utilizing this advanced material. Addressing the issue of drying shrinkage cracking observed on the UHPC deck layer of a cable-stayed bridge, a real-time investigation into crack evolution was conducted. This study employed acoustic emission (AE) technique with in-situ data processing, focusing on AE time series analysis. Additionally, triangulation techniques were utilized to determine the AE source positions of active cracks. The results showed continuous crack evolution on the UHPC deck layer, mainly due to construction vehicles, with two major instances of crack propagation and arrest. AE signals correlated with measured crack propagation, with two major AE events matching recorded crack jumps. Later AE sources indicated a step-by-step crack tip advancement. This paper underscores the effectiveness of the AE technique for crack identification and real-time monitoring of in-service bridges.

1. Introduction

The primary role of the bridge deck layer is to directly support, distribute, and transfer the wheel loads to the main girder of the bridge. The steel bridge deck is typically constructed from the orthotropic steel deck (OSD), which is lightweight, and has high load-bearing capacity and notable overloading capability. With the advancement of ultra-high performance concrete (UHPC), the orthotropic steel-UHPC composite decks are now extensively used in various bridge structures of different spans, particularly in long-span cable-stayed bridges (Zhu et al., 2023; Li et al., 2023).

The UHPC is a pioneering cement-based composite material initially developed by French scholars (De Larrard and Sedran, 1994), and mainly comprises cement, fine aggregate, fibre, silica fume, and water reducer, designed following the principle of maximum compactness (Kang et al., 2024; Huang et al., 2024). The objective is to reduce internal pores and micro-cracks, achieving excellent load-bearing capacity and durability. When the UHPC is poured and cured on the OSD, the UHPC layer is combined with the OSD using shear studs to form steel-UHPC composite decks. This composite deck significantly enhances the stiffness of bridge decks, thus preventing fatigue cracking of the OSD and deck layer damage. In recent years, the UHPC deck layer has been rapidly applied in both newly built and existing bridges, as reported in (Cao et al., 2017; Zhu et al., 2018).

Even with a low water-cement ratio, the UHPC layer on the steel deck plate is prone to losing water during the curing process, which may cause shrinkage cracks, eventually reducing its strength and durability. As a result, monitoring the entire process of cracking initiation, propagation and arrest in structural components during the bridge's service period is crucial to ensure its safety. Acoustic emission (AE) technique, which has advantages including online monitoring, internal crack position, and early damage warning, can be applied to field monitoring of large engineering structures, especially long-span cable-stayed bridges. The AE phenomenon, which involves the generation of transient elastic waves within a material by the rapid emission of localized stress energy, can be considered in the context of Fracture Mechanics (Carpinteri et al., 2016; Zhu et al., 2024). AE technique provides a non-destructive monitoring method to detect the damage evolution in materials and structures (Han et al., 2019; Lacidogna et al., 2020; Wang et al., 2024; Jiang et al., 2024a, 2024b). AE method gives a promising solution to locate and identify the crack position and type (Chen et al., 2023). AE waves can be detected by sensors placed on the structural surface,

* Corresponding author.
** Corresponding author.
E-mail addresses: 19zhjiang@stu.edu.cn (Z. Jiang), zhuzw@stu.edu.cn (Z. Zhu), giuseppe.lacidogna@polito.it (G. Lacidogna).

https://doi.org/10.1016/j.dibe.2025.100697
Received 5 April 2025; Received in revised form 19 June 2025; Accepted 21 June 2025
Available online 22 June 2025

providing crucial information on the position and crack opening mode (Aggelis et al., 2011; 2019; Carpinteri et al., 2011; 2016; Colombo et al., 2003; Shiotani et al., 1994). Various AE analysis methods have been used to characterize damage in case studies involving engineering structures, as reported in (Aggelis et al., 2013; Anzani et al., 2007; Carpinteri, 2007; Shiotani et al., 2015; Zhu et al., 2025).

Low water-to-cement ratios (typically around 0.2 or lower) of UHPC often lead to partially hydrated binder within the mortar, resulting in significantly increased autogenous shrinkage (Wu et al., 2017), up to an order of magnitude greater than that of conventional concrete (Soliman and Nehdi, 2014). Consequently, total shrinkage strains, including both autogenous and drying shrinkage, are expected to be higher than in conventional concrete. This is critical, as high early-age shrinkage strains may lead to early-age cracking (Sobuz et al., 2016; Wang et al., 2015). Recently, researchers have carried out a series of laboratory tests to investigate the cracking problem in UHPC, primarily driven by autogenous shrinkage under restrained conditions, as reported in (Du et al., 2024; Liu et al., 2022; Tutkun et al., 2023; Xie et al., 2018). While drying shrinkage is generally limited in UHPC due to its dense microstructure, extreme drying scenarios may induce minor surface cracks, as observed in tests (Xie et al., 2018; Valipour and Khayat, 2018). In the structural application of bridge decks, the early drying shrinkage of the UHPC deck layer can lead to UHPC cracking and affect the structural stability, scholars have investigated the drying shrinkage and cracking sensibility of steel-UHPC composite decks (Teng et al., 2021; Zheng et al., 2023). However, those studies were carried out in laboratories, and investigations of drying shrinkage cracking of the UHPC deck layer based on actual bridge structures have not been reported.

To fill the gap in existing research, this paper examines a real long-span bridge currently under construction, focusing on the issue of drying shrinkage cracking in the UHPC deck layer. The study utilizes AE field monitoring to address this challenge and introduces an active method for crack identification and tracking. It showcases the application of the AE technique to investigate crack development in the UHPC deck layer situated at the centre of the main span of the cable-stayed bridge. Notably, initial drying shrinkage cracking, marked by the emergence of fresh transverse cracks, has already been identified on the UHPC deck layer.

The cracking area in the UHPC, located at the centre of the main span on the southbound side, is monitored using strategically placed AE sensors. In this scenario, the AE technique facilitates the detection of crack propagation by positioning sensors near the active macro-cracks. A multi-channel AE monitoring system analyzes the temporal progression of the cracks. Damage assessment in the monitored region is performed using AE β_t and b-value analyses, along with triangulation techniques to determine the locations of active cracks (Carpinteri et al., 2011). The correlation between recorded AE activity and measured crack propagation underscores the efficacy of the AE technique for assessing crack evolution in bridge structures.

2. Overview of test bridge and UHPC deck layer

2.1. Structural information of bridge

The Niutianyang Bridge (see Fig. 1), located in Shantou, Guangdong Province, China, is a long-span cable-stayed bridge with two cable towers and a main span of 468 m crossing the Rongjiang River, as shown in Fig. 2. The bridge main girder is a steel truss incorporating with the OSD, providing highway traffic on the upper deck and urban rail on the lower deck. Three traffic lanes with a shoulder in both directions are arranged on the upper deck. Fig. 3 shows the cross section of steel truss girder. The OSD, consisting of the deck plate, U-ribs and floorbeams, is welded to the upper chord of the truss and supported by the transverse and longitudinal connection system of the truss girder. Fig. 4 shows the steel–UHPC composite decks. The steel deck plate is composited by the cast UHPC layer, with short shear studs welded to the deck plate and embedded in the UHPC, as shown in Fig. 4(a). Double-layer bidirectional (longitudinal and transverse) steel bars are placed in the UHPC. The steel material used is Q345qD, and the thickness of the steel deck plate is 16 mm, composited by 5 cm thick UHPC layer overlaid with 4 cm thick SMA-13 asphalt pavement (Fig. 4(b)). Fig. 5 shows the main construction process of the UHPC deck layer. Table 1 presents the detailed timeline for UHPC construction. The steam curing technique can promote the final strength of the UHPC layer in a short period and reduce the shrinkage and creep of the UHPC material after service. Currently, the structural construction is almost completed, since the UHPC deck layer is finished, with only the SMA pavement layer waiting for construction.

The FEM of the bridge is established in ANSYS (Fig. 2). In the coordinate system, the x-axis lies in the longitudinal bridge direction, with the y-axis in the transverse direction and the z-axis in the vertical direction. In this model, the beam elements are used to simulate the steel truss girder and the main towers, and the link elements are used to model the cables, with the shell elements for the steel bridge deck and the UHPC layer. The piers are also simulated using beam elements, with bearings presented to support the steel truss girder at its intersection with the cable towers. Young's modulus of 2.06×10^5 MPa and 3.4×10^4 MPa, and Poisson's ratio of 0.3 and 0.2 are used for the steel and concrete materials of the bridge, respectively. All degrees of freedom at the base of both the piers and the cable towers are constrained. Fig. 2 shows the stress results of the bridge deck under the dead load. The test area is the UHPC deck layer near the span centre, which is in tension, and may suffer from cracking, as indicated by the FEM results (Fig. 2).

2.2. UHPC material used in bridge deck

The UHPC mix used in the deck is listed in Table 2. Steel fibres with a length of 12 mm, a diameter of 0.2 mm, and a tensile strength higher than 3000 MPa, are mixed considering a fibre volume fraction equal to 2 %. The UHPC specimens were cured using steam conditions, and the

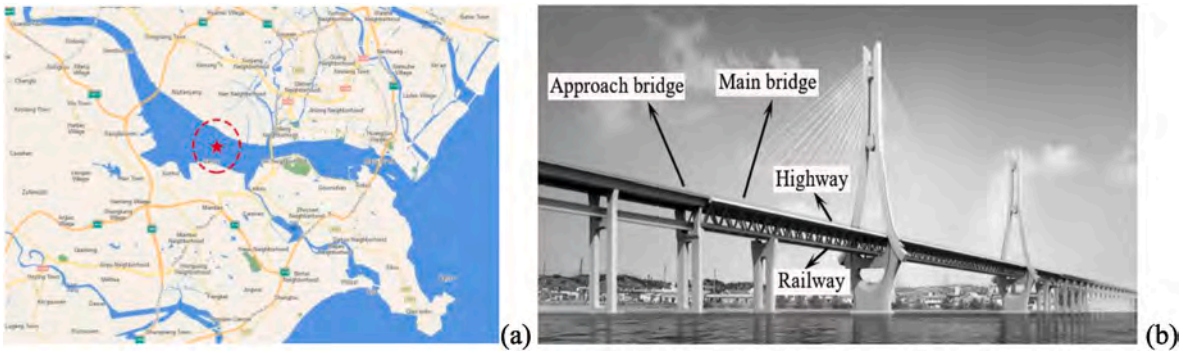

Fig. 1. The monitored bridge: Localization of the bridge on map (a). Bridge photo (b).

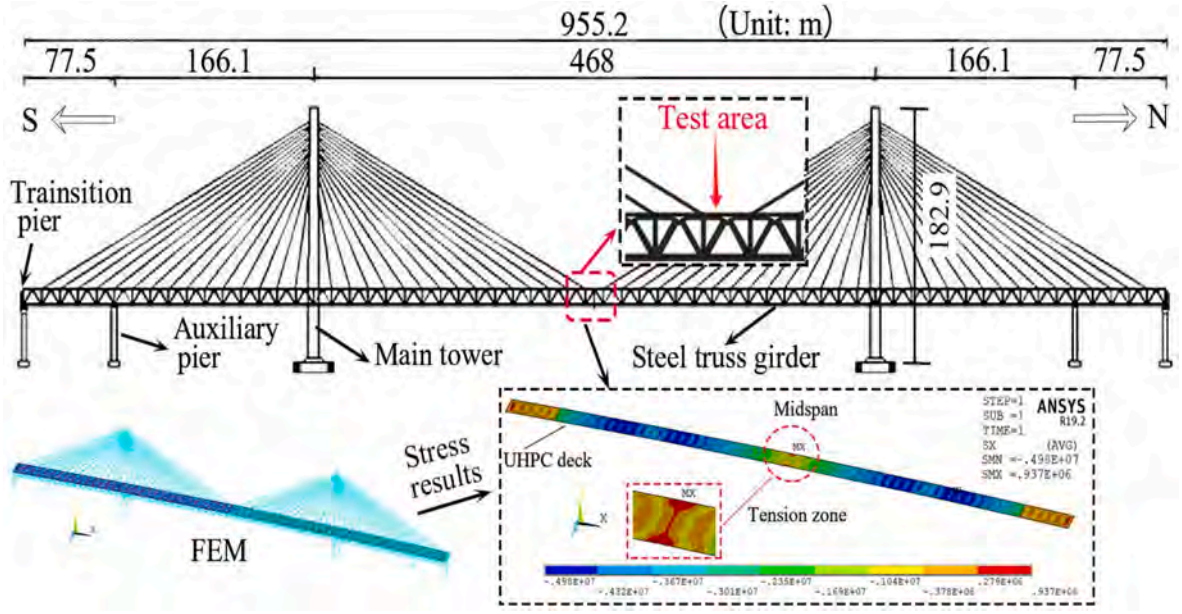

Fig. 2. Elevation layout and finite element model of the monitored bridge.

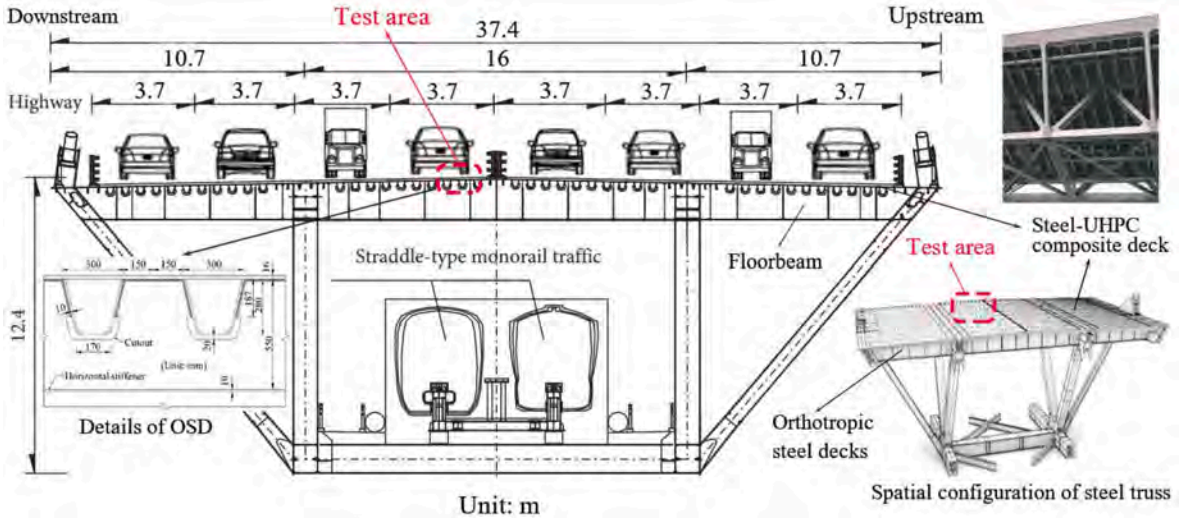

Fig. 3. Standard cross section and details of steel truss girder.

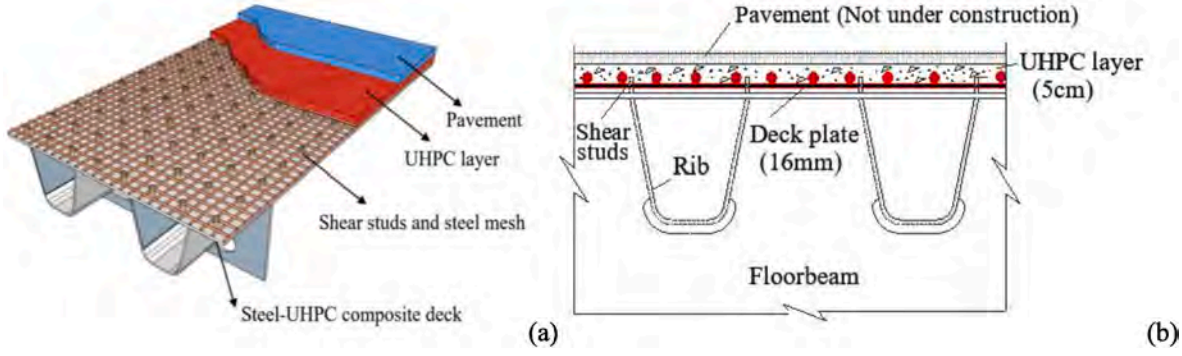

Fig. 4. The orthotropic steel–UHPC composite deck: Cross section (a). Stereogram (b).

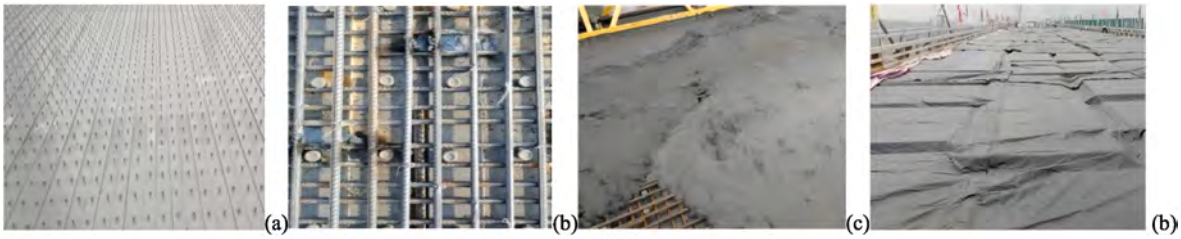

Fig. 5. UHPC construction process: Welded shear studs (a); Steel mesh (b); Pouring (c); Steam curing (d).

Table 1
Detailed timeline for UHPC construction.

Construction phase	Completed casting	Initial setting	Beginning of steam curing	Final setting	End of steam curing	First crack observation
Time	Day 1, 9:00	Day 1, 12:00	Day 1, 16:00	Day 1, 22:00	Day 3, 13:00	Day 6, 14:00

Table 2
UHPC mix (kg/m^3).

Component	Cement	Silica ash	Fly ash	Quartz sand	Water	Steel fibre	Polycarboxylate water reducer
Dosage	850	137.5	112.5	1100	198	234	17.1

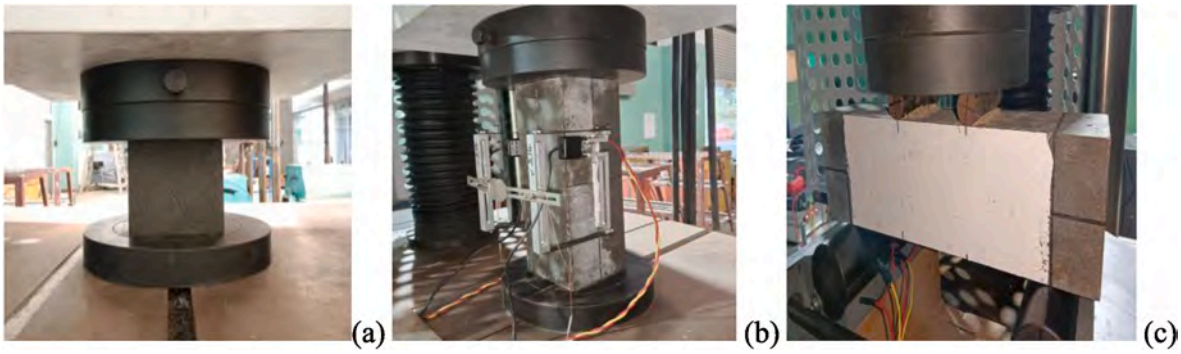

Fig. 6. Preliminary tests of UHPC: Compression (a), (b); Bending (c).

Table 3
UHPC mechanical properties.

Material	Compression strength (MPa)	Elastic modulus (GPa)	Flexural strength (MPa)
UHPC	131.1	44.3	10.8

UHPC preliminary tests to characterize the material are depicted in Fig. 6, whereas test results are listed in Table 3.

2.3. Observed drying shrinkage crack and test area

As mentioned earlier, steam curing is usually used to reduce shrinkage during the curing process. However, since the end of UHPC construction, emerging drying shrinkage cracks have been observed on the UHPC deck layer in the main span centre at the south bound (Fig. 7), showing a transverse bridge crack easily observed by the human eye, as shown in Fig. 8(a). The test area is shown in Figs. 7 and 8, where in the bridge longitudinal direction, it is at the middle way of two transverse floorbeams of the OSD.

In recent days, the crack has increased to a length extending over 30 mm. Temperature effect and traffic disturbance may result in further crack propagation on the UHPC deck layer in certain conditions. In order to identify the crack activity and its potential propagation, the cracked UHPC on the test area is subjected to AE monitoring (see below).

3. AE field test

3.1. Monitoring system

The growing need for continuous monitoring of bridges requires wireless transmission, enabling real-time observation to identify the ongoing degradation processes (Manuello et al., 2019). In this context, the Italian company Lunitek has developed the ÆMISSION® system, which utilizes AE data acquisition and wireless transmission (Fig. 9). Piezoelectric sensors (range: 10 kHz-1MHz) are connected to the data acquisition device (Fig. 9(a and b)), automatically storing waveform parameters and allowing the damage location from the detected data, which is sent to a remote server through the GPRS system.

The monitoring scheme of the AE system is shown in Fig. 9(c), each channel features an analog digital converter (ADC) with a sampling rate of 10M samples/s. Digital signals are then parallelly acquired and processed by the FPGA, according to the defined parametrization, only the signals that satisfy the setting parameters are transferred to the Linux CPU. Inside the Linux CPU signals are stored locally and can be shared remotely via WiFi or a 4G connection.

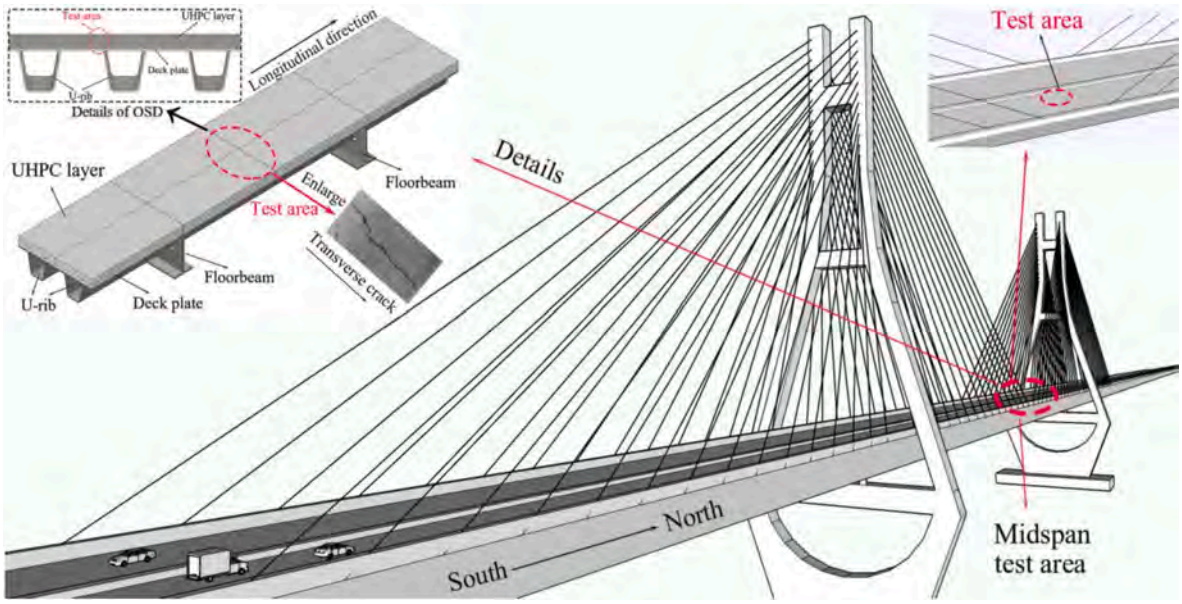

Fig. 7. Main bridge 3D diagram and test area location.

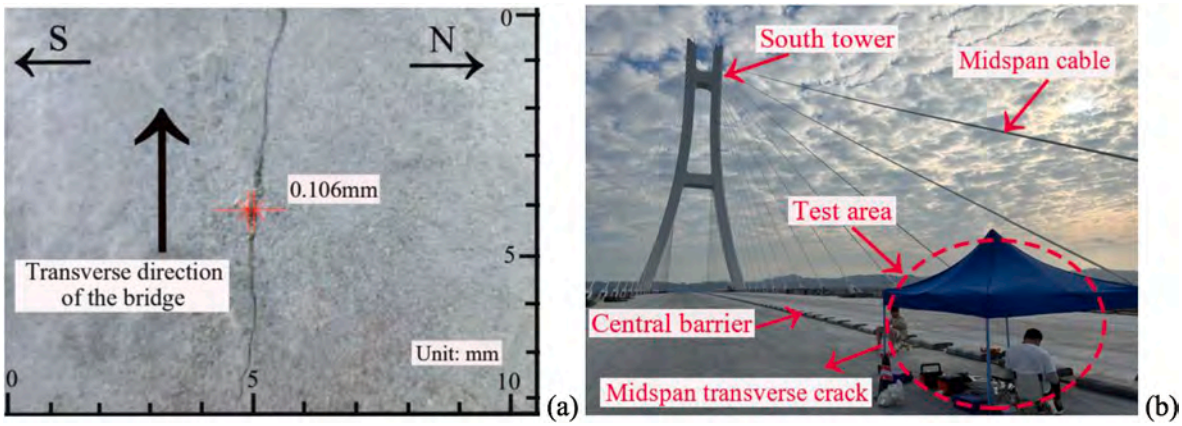

Fig. 8. Field monitoring: Cracking pattern on UHPC deck layer (a). On-site photo (b).

3.2. AE test layout

AE sensors are glued with silicone resin and positioned on the test area of the UHPC deck layer. The positioning of AE sensors is shown in Fig. 10. Four sensors are used to determine the location of the AE sources.

Most of the ambient noise can be filtered out in the test by setting a reasonable threshold. Before the start of monitoring, the background noise is examined over a representative period (i.e., 3h) to determine the level of spurious signals. By statistically analyzing the peak amplitudes of all noise signals during this period, we found that the amplitude distribution of the background noise follows a normal distribution, with a mean of $\mu = 1.2$ mV and a standard deviation of $\sigma = 0.3$ mV. Based on the 3σ principle, we set the threshold at 2 mV to maximize noise suppression. Through the analysis of the frequency of background noise signals that exceed the threshold (2 mV), we calculated a false positive rate of 0.5 % (meaning only 1 out of every 200 noise signals exceeds the threshold). This indicates that the threshold setting effectively distinguishes between noise and valid signals.

Post-process analysis has filtered out possible voltage spikes (i.e., signals with duration < 3μs and counts number <3), as well as possible low-frequency structural vibrations (i.e., signals with frequency <20 kHz). The analysis of background noise using a fast Fourier transform revealed that the majority of noise energy is concentrated in the frequency range below 20 kHz, while the AE signals related to crack propagation typically fall within the 50–400 kHz range. In terms of low-frequency vibration filtering (<20 kHz), comparing the AE signals rates before and after filtering showed that low-frequency noise signals decreased by 82 %, while the retention rate of crack-related signals (>50 kHz) was 95 %, demonstrating the effectiveness of the filtering criteria. The analysis of short-duration signal filtering (<3 μs) indicated that such signals accounted for 12 % of the background noise, but none were found to be temporally or spatially associated with crack propagation signals, suggesting that these signals may have originated from electromagnetic interference or transient mechanical impacts.

The local vibrations of the bridge caused by wind loads can generate low-frequency, low-amplitude AE signals. When vehicle loads pass over, vibrations from other components may transfer to the UHPC layer, producing low-frequency AE signals. Non-crack-related AE signals within the UHPC include high-frequency, low-energy signals from fibre-matrix interface delamination and low-frequency micro-cracking signals induced by temperature strain. Data indicates that when wind speeds exceed 8 m/s, the rate of low-frequency noise signals increases by 25 %. However, after applying a 20 kHz filter, these signals are almost completely eliminated (residual rate <1 %). According to the bridge dynamic weighing system, the low-frequency vibration signals (10–30

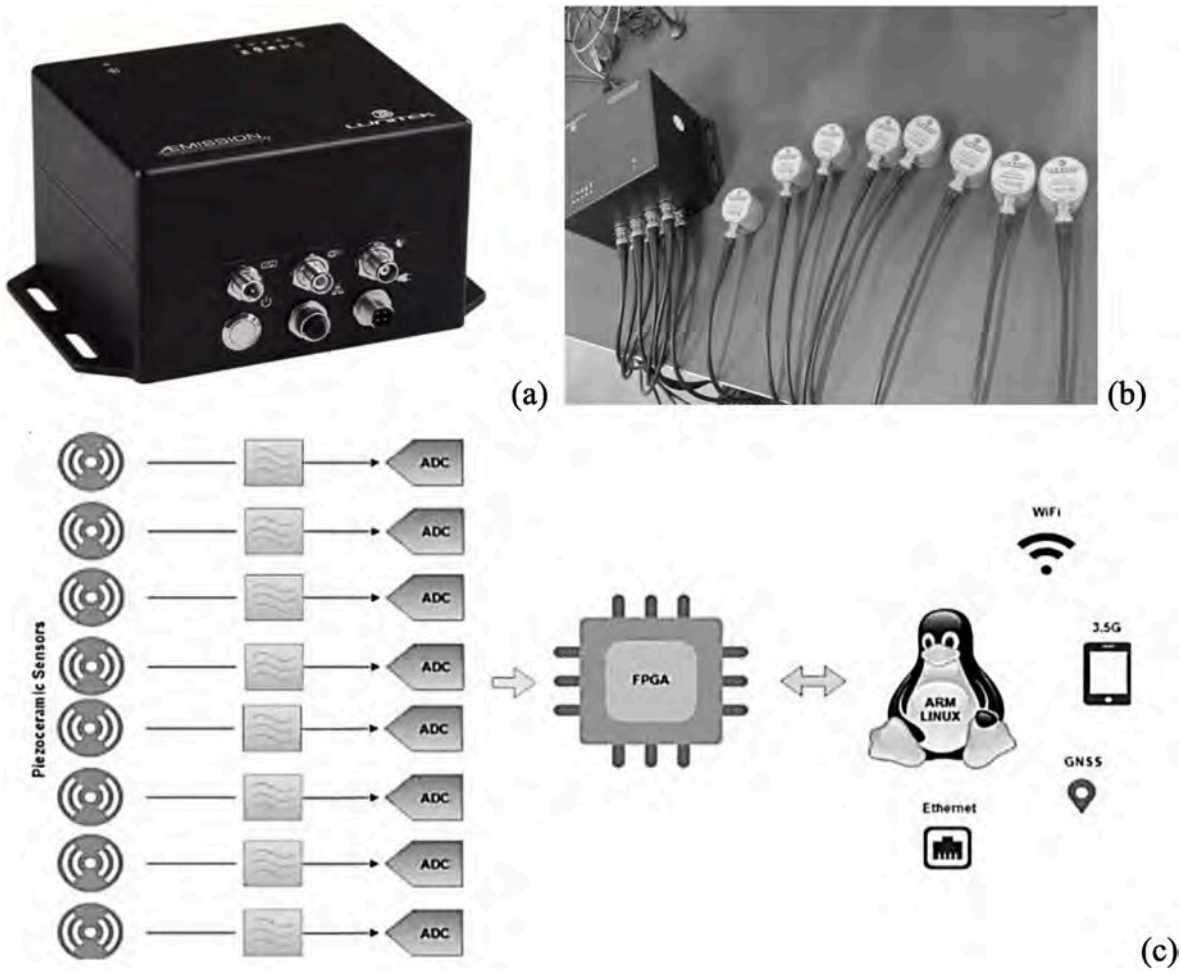

Fig. 9. AE acquisition device and sensors (a), (b). Monitoring scheme of AE system (c).

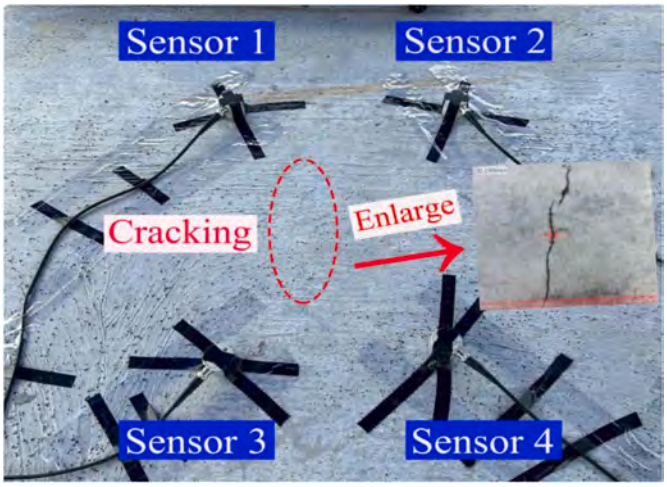

Fig. 10. Layout of the AE sensors on the UHPC deck layer.

kHz) generated during vehicle passage account for 18 % of the background noise, but their influence is negligible after applying threshold and frequency filtering. Based on the background noise statistics (mean of 1.2 mV and standard deviation of 0.3 mV), a threshold of 2 mV can filter out 99 % of environmental noise. High-pass filtering (>20 kHz) effectively suppresses wind noise and vehicle vibration noise, increasing the proportion of crack-related signals from 68 % to 92 %. This study effectively reduces the risk of false positives from wind loading, component vibrations, and non-crack-related AE signals through threshold setting and frequency filtering.

3.3. AE time series and AE response analysis

The results of the AE data for the entire monitoring period are illustrated in Fig. 11, and the AE analysis is based on the data recorded on the test area of the UHPC deck layer, from 3:00 to 6:45 p.m. on October 23, 2023. Although the AE monitoring was conducted over a much longer period, during this chosen time period window, crack propagation and eventual arrest were clearly observed in the targeted area.

The *b*-value characterizes the scaling of AE amplitude distribution according to the Gutenberg and Richter law, $N(\geq A) \sim A^{-b}$, where A is the signal magnitude and N represents the number of AE signals with a magnitude exceeding A (Shiotani et al., 1994). The coalescence of micro-cracks causes higher amplitude signals, leading to a decrease in *b*-value to 1 or lower (Guzmán et al., 2015; Ohtsu, 2015).

The damage evolution is caught by the β_t coefficient in the power-law relationship, $N(t) \sim t^{\beta t}$, where $N(t)$ is the cumulated AE signals up to the time t (Carpinteri et al., 2006). Results of $\beta_t < 1$ indicate a gradual decrease in AE signals over time, suggesting stable conditions. In contrast, results of $\beta_t < 1$ are signatures of structural instability, indicating the rapid damage progression. The β_t value of 1 is seen as a meta-stable state, which can progress toward either stability or instability, as reported by (Carpinteri et al., 2011).

The two diagrams (Fig. 11(a and b)) depict the cumulated AE signals

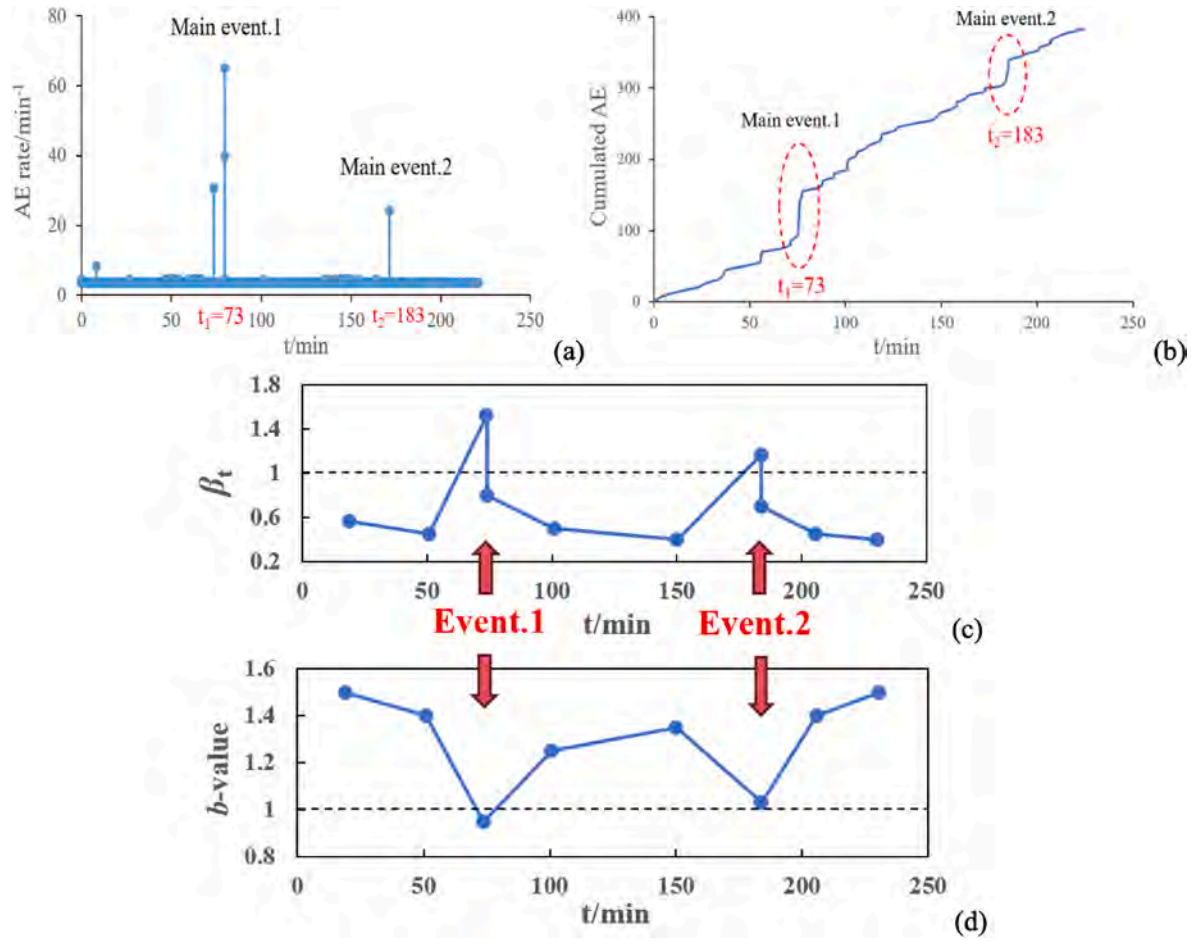

Fig. 11. AE time series results: AE signals rate (a). Cumulated AE signals (b)AE β_t coefficient and *b*-value (c), (d).

and the AE rate (AE signals per minute) over time, indicating the occurrence of irreversible damage in the monitored areas. By cutting the AE data into sets of 50 signals, the trends of β_t coefficient and *b*-value (Fig. 11(c and d)) can be correlated with the cumulated AE diagrams. The steady damage accumulation rate is disturbed by a main sharp acceleration with up to 60 signals per minute at the 73rd minute, followed by a sub-sharp acceleration with up to 30 signals per minute at the 183rd minute (Fig. 11(a and b)), as evidenced by the evolution of two monitoring indicators derived from AE time series, i.e. the β_t coefficient and *b*-value (Fig. 11(c and d)).

During the initial 50-min monitoring period, the β_t coefficient hovers around 0.5, with the *b*-value declining but remaining within the range of 1.4–1.5, suggesting micro-cracking regimes. The following increase of β_t coefficient to 1.5, along with the corresponding decrease of the *b*-value to a critical value near 1 coincides with the sudden rise in AE signals (Fig. 11(a and b)) observed at the 73rd minute and 183rd minute. The β_t coefficient equal to 1.5 (peaks in Fig. 11(c)) indicates unstable crack evolution, and the *b*-value close to 1.0 (minimum in Fig. 11(d)) signifies the stage of macro-crack propagation. Therefore, the two main AE events corresponding to macro-crack propagation are monitored through the AE monitoring system.

The UHPC mechanical properties, including high strength and a dense microstructure, significantly influence the characteristics of AE responses. This influence is primarily reflected in changes in crack propagation patterns, energy release mechanisms, and background noise. The high strength of UHPC leads to a more abrupt crack propagation process and a more concentrated energy release. Compared to ordinary concrete, when cracks propagate rapidly, the energy release of elastic waves is more intense, which may result in an increased proportion of high-amplitude AE signals and a corresponding decrease in the *b*-value (which reflects the increase in the proportion of large signals). This phenomenon is consistent with the observation in experiments that *b*-values drop to around 1.0 during the critical stage of crack propagation (see Fig. 11(d)). Additionally, the brittle characteristics of the UHPC matrix may cause cracks to transition more rapidly from stable propagation (micro-crack) to unstable propagation (macro-crack), as indicated by a significant increase in β_t coefficient over a short period (see Fig. 11(c)), reflecting the rapid accumulation of damage. The low porosity and uniform microstructure of UHPC also reduce the AE noise sources unrelated to cracks (such as pore collapse and aggregate interfacial debonding), thus improving the signal-to-noise ratio of the AE signals. This makes it easier to accurately capture crack-related AE signals (such as fibre debonding and matrix cracking), further supporting the high correlation between AE parameters and crack propagation observed in the experiments (see Fig. 12).

3.4. Crack evolution by field measurement

As shown in Fig. 12(a), increases in crack opening and crack tip advancement are observed during the monitoring period (caused by truck traffic, see section 3.6 below). Crack width and length are measured in the field with instruments from Beijing ZBL Sci & Tech. The data is measured every 20 min, and the results are shown in Fig. 12(b).

It is observed that the two main events detected by the AE monitoring system (Fig. 11) correspond to the two major jumps in the diagrams of the measured cracks (Fig. 12(b)). Furthermore, the greater the increase of the AE signals, the greater the jump of measured cracks. The results indicate a strong temporal correlation between measured crack

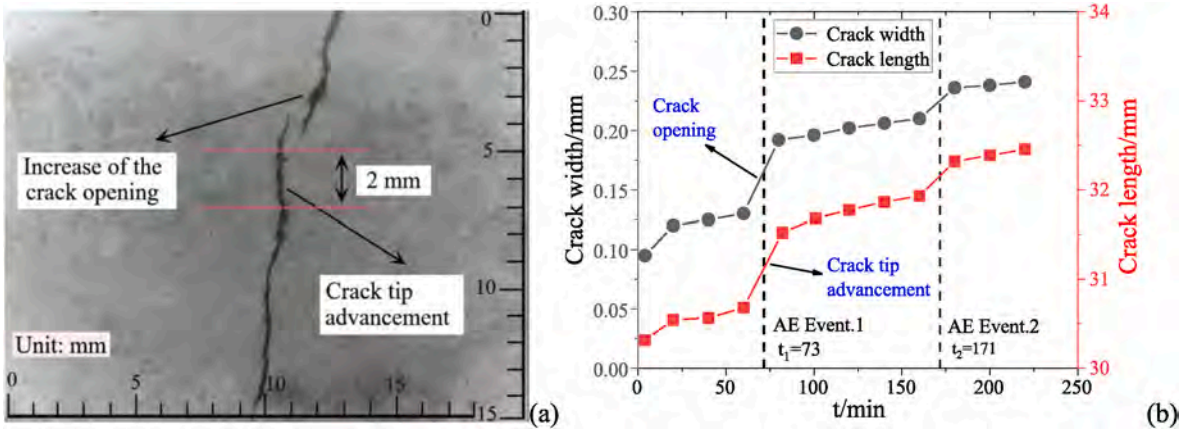

Fig. 12. The crack curve measured in the field.

propagation and AE monitoring signals.

3.5. AE source position

Localization of AE sources is crucial to identify the regions of active cracks in the monitoring technique. As reported in (Carpinteri et al., 2012; Ge, 2003a, 2003b; Niccolini et al., 2019), position problems are analyzed using the triangulation governing equation, which is solved through iterative techniques that employ classical Least Squares and Gauss-Newton methods in the AE system. AE events are located by

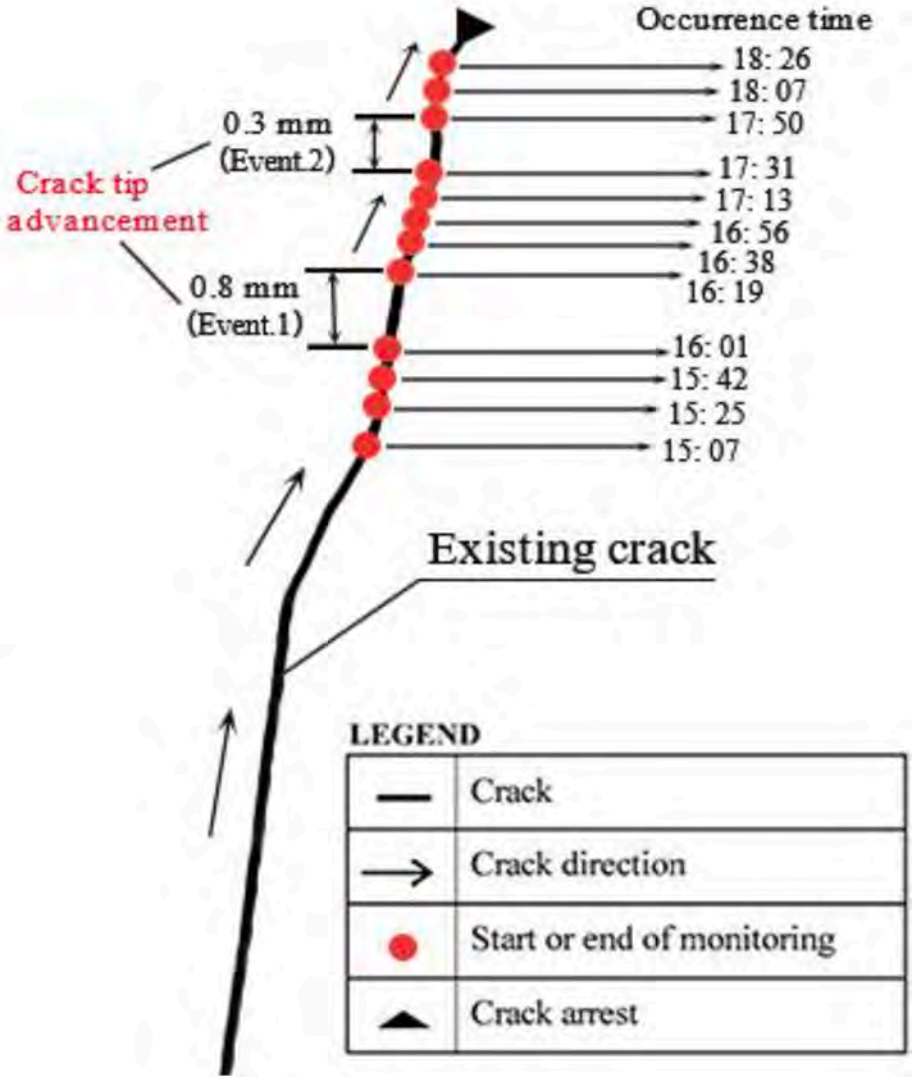

Fig. 13. Crack tip advancement trace positioned by AE sources (red points).

determining the exact position of the sensors and calculating the difference in signals arrival times among them.

In the application of AE triangulation techniques, we optimized sensor placement to enhance localization accuracy. We adopted a multi-point layout strategy, forming a quadrilateral structure to improve signal coverage and redundancy while minimizing sensor spacing for better geometric distribution. Through multiple trials, we determined the optimal sensor spacing to avoid signal interference and strength reduction. Additionally, background noise analysis helped us identify unsuitable areas for sensor placement, further refining the layout. Finally, data processing utilized signal threshold settings and time-difference measurements to enhance localization accuracy and reduce errors caused by environmental factors. These optimizations significantly improved the accuracy of AE source localization.

The results of the AE source position procedure (red dots) are illustrated in Fig. 13, which outlines the advancement of the crack tip, with red dots moving upwards indicating a step-by-step advancement of the crack tip. This evidence is in good agreement with the cracking pattern measured in the field (Fig. 12). The position of AE sources by triangulation techniques allows the localization of active crack tips like those indicated by Event.1 in Fig. 12(b), localized after the 73rd minute from the beginning of the monitoring, then by Event.2, subsequently localized on the 183rd minute (Fig. 12(b)), and the crack arrest at last (Fig. 13). It can also be noticed that the two more widely spaced AE sources represent two main events, signalling two rapid advancements of the crack tip. These two main AE events from the AE source position are compatible with the transverse propagation of the crack measured in the field.

3.6. Analysis of crack propagation

The data collected during the monitoring period are analyzed to evaluate crack propagation and correlate it with the other phenomena considered, such as the vehicle traffic on the bridge deck and earthquake occurrence in the bridge site. The monitoring process reveals an ongoing damaging process, characterised by crack propagation with two main sudden accelerations of the process on the UHPC deck layer. The discontinuities in the cumulated AE curve denote the critical moments during which the release of energy from the micro-crack formation process is greatest.

In view of a magnitude 5.0 earthquake taking place locally in Shantou City at 03:20 a.m. on the monitoring day (23 October). As a result, frequent aftershock activity occurred at the bridge site during the monitoring period. As shown in Fig. 14(a), AE monitoring and regional earthquake data, within a radius of 20 km around Shantou city, reveal no statistical correlation between the AE activities determined experimentally and seismic events. Moreover, it could be observed that an AE burst does not follow each seismic event. The comparison between the two distributions reveals that, during the monitoring period, the earthquake effects on the damage to the bridge decks are negligible.

Fig. 14(b) shows the AE and vehicle traffic. In the diagram, the cumulated AE function relating to the monitored area is overlaid with the construction vehicles recorded on the bridge during the same period, based on data collected by the bridge management authority. In this particular case, it can be noted that two appreciable crack propagation, i.e., the sudden increases of the cumulated AE in the zone monitored, are strongly correlated with two truck traffic peaks, and the cumulated AE curves grow rapidly immediately after the traffic peaks. Thus, it can be confirmed that the vehicle traffic mainly causes the rapid increase of the UHPC crack during the monitoring period. In addition, the decrease in temperature can result in the contraction of the bridge main girder, and the produced tensile stress may further cause crack propagation on the UHPC deck layer.

Nowadays, before the construction of bridge deck pavement, the bridge UHPC deck layer is usually open to construction vehicles, and the vehicle traffic can lead to the UHPC deck layer reciprocating flexural deformation and vehicle-bridge coupling vibration. However, once the drying shrinkage cracks appear on the UHPC deck layer due to improper construction, traffic disturbance and temperature effects may cause further crack propagation, eventually posing a risk to the long-term durability of the bridge structures. Consequently, identifying the crack activity and monitoring the process of crack evolution on the UHPC deck layer during the bridge's construction is crucial to ensure its safety, and AE technique can provide an effective method for the identification and real-time monitoring of active cracks.

4. Discussion

4.1. Mechanical analysis of the UHPC mix

The mechanical properties of UHPC are determined by its high-density matrix and fibre reinforcement effects, which significantly influence crack propagation behaviour and the characteristics of accompanying AE signals. Materials such as cement, silica fume, and quartz sand in UHPC form a high-strength matrix with a low porosity (<2 %) through dense packing (with a compressive strength of 131.1 MPa and an elastic modulus of 44.3 GPa). The volume fraction of steel fibres is 2 %, with a tensile strength exceeding 3000 MPa, providing effective crack bridging and mechanical reinforcement. The bridging effect of the fibres delays crack propagation, resulting in significantly higher fracture energy for UHPC compared to ordinary concrete. The cracking process of UHPC involves a multi-stage failure, including a microcrack formation stage (elastic stage), a stable propagation stage (fibre bridging stage), and an unstable fracture stage (fibre pullout stage).

In UHPC, steel fibres serve a bridging role, and their interfacial debonding and pullout can significantly alter the characteristics of AE

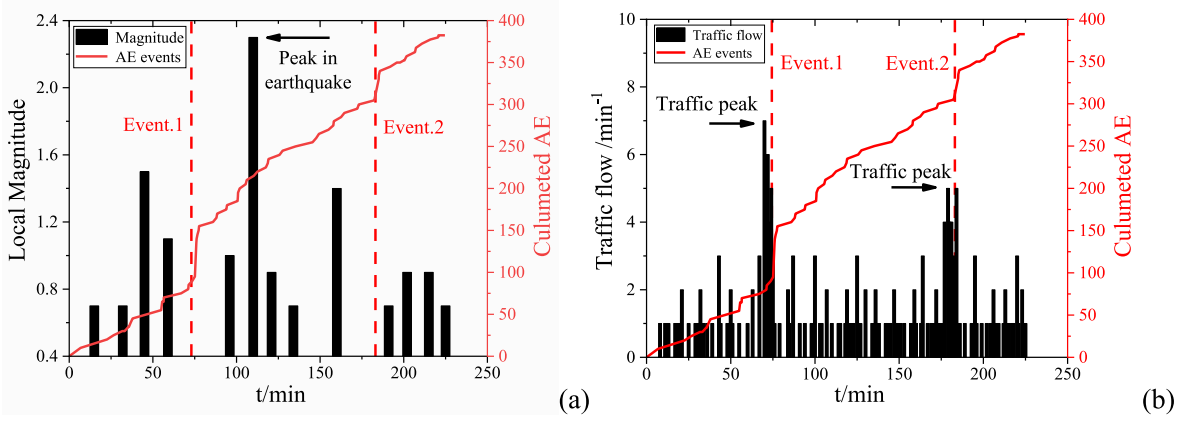

Fig. 14. Analysis of AE and environmental effects: AE and earthquakes (a). AE and vehicle traffic (b).

signals, affecting the amplitude distribution of AE signals (*b*-value) and the signals accumulation pattern (β_t coefficient). In the microcrack stage, the debonding of fibres at the matrix interface produces high-frequency, low-amplitude AE signals, primarily contributing to the initial linear growth phase of AE signal accumulation (see Fig. 11(b)), resulting in a higher *b*-value during the early stages of crack propagation (with the experimental initial *b*-value around 1.4–1.5, see Fig. 11(d)). In the macroscopic crack stage, the gradual pullout of fibres is accompanied by a significant number of mid-to low-amplitude signals, while the sudden penetration of the main crack generates high-amplitude signals. This mechanism explains the observed correlation between the stage-wise decrease in *b*-values and the crack propagation events in the experiments (such as the *b*-value troughs at the 73rd and 183rd minutes).

The high-density matrix of UHPC reduces initial defects, thereby delaying the formation of microcracks. The amplitude of matrix cracking signals is relatively high (>40 dB), but the frequency is low, reflecting the brittle fracture characteristics of the matrix, leading to a concentrated outburst of AE signals during the unstable phase. The brittle fracture of the matrix interacts with the ductile response of the fibres, resulting in a "stepped" crack propagation pattern (see Fig. 12 (b)). In the alternating process of crack propagation being hindered (fibre bridging) and breaking through (fibre pullout), the rate of AE signals exhibits a pulsed increase (as seen in the peaks at the 73rd and 183rd minutes, see Fig. 11(a)). The abrupt increase in β_t during the unstable phase (peak value of 1.5, see Fig. 11(c)) is associated with the rapid cracking of the matrix and fibre failure.

4.2. Potential mechanisms of crack arrest in UHPC

The mechanisms for crack arrest in UHPC result from the synergistic action of fibre bridging, residual tensile strength, and compressive stress redistribution.

UHPC typically incorporates short fibres, which create a bridging effect within the concrete. When a crack occurs, these fibres provide tensile forces on either side of the crack, offering additional mechanical restraint that delays crack growth. The distribution, shape, and orientation of the fibres within the microstructure of the crack significantly influence the degree of this bridging effect, enhancing the toughness and crack resistance of UHPC. This fibre bridging effect helps to improve the material's fracture toughness and promotes crack stagnation.

UHPC possesses high compressive strength and designed residual tensile strength. Even after cracking, the material retains some tensile capacity, preventing instantaneous crack propagation. Additionally, UHPC mixtures often include mineral admixtures (such as silica fume), which significantly enhance the residual tensile strength of the concrete through their synergistic effects on the cement matrix, thereby inhibiting further crack extension to a certain degree.

The formation of cracks in UHPC can lead to changes in the internal stress distribution of the material. Specifically, when a crack appears, the surrounding areas may experience a redistribution of compressive stress, exerting additional compressive forces on the new crack surfaces. This compressive stress redistribution can help suppress crack growth and create a form of "self-healing" mechanism at the crack edges, particularly under suitable humidity and environmental conditions, where micro-cracks may regenerate through the cementitious matrix.

In summary, the mechanisms for crack arrest in UHPC are multi-faceted, primarily depending on the intrinsic structural characteristics of the material and the loading conditions. Future research could further quantify the contribution of each mechanism and explore new fibre types and matrix modification techniques to optimize crack arrest effects.

4.3. Limitations of AE monitoring

While the AE technique demonstrated effectiveness in tracking crack evolution in the UHPC deck layer, there are several limitations that deserve discussion in order to guide future applications.

The study employed a 2 mV threshold and high-pass filtering (>20 kHz) to minimize false positives. Statistical analysis of background noise revealed a false positive rate of 0.5 % (1 in 200 noise signals exceeding the threshold). However, transient disturbances (e.g., electromagnetic interference or mechanical impacts) could still generate short-duration signals (<3 μs) unrelated to cracks. Post-processing excluded these signals, but their presence underscores the need for adaptive thresholding in dynamic environments.

The quadrilateral sensor array (Fig. 10) optimized localization accuracy, but practical constraints (e.g., bridge geometry and accessibility) limited sensor density. This sensor placement is verified by comparing AE-derived crack tips with field measurements (Fig. 13). Future work could employ denser arrays or multi-modal sensing (e.g., combining AE with strain gauges) to improve resolution. Environmental noise (e.g., wind-induced vibrations >8 m/s or vehicle traffic) contributed to low-frequency (<30 kHz) signals, which were suppressed by high-pass filtering. While filtering retained 92 % of crack-related signals, it may attenuate low-frequency AE events from micro-crack initiation. The β_t and *b*-value trends (Fig. 11) indirectly validated filtering efficacy, but laboratory calibration under controlled noise conditions could further refine thresholds.

The results are specific to UHPC's dense microstructure and steel-fibre reinforcement, which alter AE signal characteristics (e.g., higher amplitude during brittle fracture). For other types of materials, noise profiles and crack propagation dynamics may differ, necessitating tailored filtering strategies.

4.4. Comparison with other non-destructive techniques

AE testing demonstrates unique advantages for structural crack monitoring, particularly for real-time detection of internal micro-crack initiation and propagation, even before surface visibility. Its triangulation capability enables precise crack tip tracking (Section 3.5), while high-frequency sensitivity makes it ideal for dynamic loading scenarios like traffic-induced cracking. In contrast, Digital Image Correlation (DIC) provides superior surface-level quantification of crack openings and strain fields, offering complementary data to AE's subsurface detection. The synergistic potential of these methods has been demonstrated by Lacidogna et al. (2020).

Compared to strain gauges, AE offers superior spatial coverage by monitoring distributed damage events across entire structures, rather than localized strain at discrete points. AE's dynamic parameters (β_t and *b*-value variations in Section 3.3) can identify active crack growth, while strain gauges merely record cumulative deformation. Practical limitations of strain gauges include insensitivity to micro-cracks unless precisely positioned, and reduced effectiveness under dynamic construction loads. Their dense deployment for equivalent AE coverage would be prohibitively costly, whereas AE's wireless system (Section 3.1) provides scalable monitoring.

For this UHPC bridge study, AE's real-time crack detection capability and resilience to construction conditions made it the optimal choice. While DIC and strain gauges were unsuitable for field deployment due to weather and traffic constraints, future laboratory studies will incorporate DIC to validate surface crack behavior, enhancing the comprehensive understanding of UHPC fracture mechanisms.

4.5. AE for long-term durability assessment

AE technology provides unique advantages for long-term structural health monitoring of UHPC bridge decks. Its early damage detection capability identifies micro-crack formation and propagation before visible signs appear (Carpinteri et al., 2016). The wireless AE system (Section 3.1) enables continuous, low-maintenance monitoring, ideal for extended durability assessment. Unlike conventional inspections, it delivers real-time damage progression data under operational loads.

Quantitative evaluation is achieved through AE parameters (b-value, β_t) that track material degradation, while cumulative energy analysis correlates with fatigue life. Additionally, frequency-domain analysis differentiates damage mechanisms, distinguishing corrosion-induced cracks from mechanical fatigue cracks by their spectral characteristics.

However, long-term AE monitoring applications face several practical limitations. Piezoelectric sensors typically degrade after years of outdoor exposure, requiring periodic replacement, while aging UHPC exhibits increasing signal attenuation. The continuous monitoring generates massive datasets (terabytes annually), demanding sophisticated data processing algorithms. Environmental challenges are particularly significant in Shantou, where >40 °C temperature variations and weather events interfere with low-energy AE signals, necessitating adaptive filtering. Long-term data interpretation grows increasingly complex, especially in differentiating structural cracks from benign micro-cracks, while regular calibration remains crucial to maintain sensor accuracy and data consistency throughout extended monitoring periods.

5. Conclusions and perspectives

Focusing on observed cracks on the UHPC deck layer of a long-span cable-stayed bridge under construction, this paper proposes an active crack identification and monitoring method to trace the crack evolution by the AE technique. The conclusions are as follows.

(1) Emerging drying shrinkage cracks have been observed on the UHPC deck layer in the main span centre after UHPC construction, exhibiting a fresh cracking pattern in the bridge transverse direction. Field test results confirm the existence of a continuous crack evolution on the test area of the UHPC deck layer, which is mainly driven by construction vehicles, with two main sudden crack propagation and the final crack arrest.
(2) Detected AE signals are consistent with the measured crack propagation in the field. Specifically, the two main events recorded by the AE system are related to the two major jumps in the results of the measured crack, i.e., crack opening and advancement, whereas a greater increase in AE signals is accompanied by greater growth in measured cracks, confirming a strong correlation between the AE signals from the cracks and the measured crack propagation.
(3) AE parameter analysis can provide a real-time monitoring method for crack evolution. The AE time series results describe a damage accumulation, with two main sudden increases (AE events) during the 73rd and 183rd monitoring minute, revealed also by abrupt changes in two AE indicators, i.e., the β_t coefficient and the b-value. The two main AE events, corresponding to a critical value close to 1 reached by the b-value, represent the signatures of significant macro-crack propagation.
(4) AE source position can trace the crack tip advancement, providing an identification method for active cracks. AE sources localized in subsequent time steps are signatures of macro-crack propagation, indicating a step-by-step advancement of the existing crack tip, while the predicted cracks are in good agreement with the measured cracks. Additionally, two more widely spaced AE sources represent two main events, signalling two rapid advancements of the crack tip.

UHPC cracking during construction may pose a risk to the long-term durability of the bridge structures. This study suggests that early detection of cracking damaging evolution in bridge structures is possible by AE monitoring, and AE technique provides an effective method for the identification and real-time monitoring of active cracks. Furthermore, an extension of monitoring areas, possibly including other segments of the UHPC deck layer, is needed to give an exhaustive assessment of the evolving crack pattern. While this study focused on construction-phase cracking, AE shows strong potential for lifelong structural health monitoring when integrated with complementary NDT methods and robust data management systems.

CRediT authorship contribution statement

Zihan Jiang: Writing – review & editing, Methodology, Investigation, Data curation, Conceptualization. **Zhiwen Zhu:** Writing – review & editing, Writing – original draft, Methodology, Investigation, Data curation, Conceptualization. **Giuseppe Lacidogna:** Writing – review & editing, Writing – original draft, Project administration, Methodology, Investigation, Funding acquisition, Data curation, Conceptualization.

Data availability statement

Some or all data, models, or code that support the findings of this study are available from the corresponding author upon reasonable request.

Declaration of competing interest

The authors declare that they have no known competing financial interests or personal relationships that could have appeared to influence the work reported in this paper.

Acknowledgements

The authors wish to acknowledge the National Natural Science Foundation of China (52278509), the International Training Program for Outstanding Young Scientific Research Talents of Shantou University, and the sponsorship guaranteed with basic research funds provided by Politecnico di Torino, Italy for their financial aids in this work.

Data availability

Data will be made available on request.

References

Aggelis, D.G., 2011. Classification of cracking mode in concrete by acoustic emission parameters. Mech. Res. Commun. 38 (3), 153–157. https://doi.org/10.1016/j.mechrescom.2011.03.007.
Aggelis, D.G., Mpalaskas, A.C., Matikas, T.E., 2013. Investigation of different fracture modes in cement-based materials by acoustic emission. Cement Concr. Res. 48, 1–8. https://doi.org/10.1016/j.cemconres.2013.02.002.
Aggelis, D.G., Sutter, S.D., Verbruggen, S., Tsangouri, E., Tysmans, T., 2019. Acoustic emission characterization of damage sources of lightweight hybrid concrete beams. Eng. Fract. Mech. 210, 181–188. https://doi.org/10.1016/j.engfracmech.2018.04.019.
Anzani, A., Binda, L., Carpinteri, A., Lacidogna, G., Manuello, A., 2007. Evaluation of the repair on multiple leaf stone masonry by acoustic emission. Mater. Struct. 41, 1169–1189. https://doi.org/10.1617/s11527-007-9316-z.
Cao, J., Shao, X., Deng, L., Gan, Y., 2017. Static and fatigue behavior of short-headed studs embedded in a thin ultrahigh-performance concrete layer. J. Bridge Eng. 22 (5), 04017005. https://doi.org/10.1061/(ASCE)BE.1943-5592.0001031.
Carpinteri, A., Lacidogna, G., 2006. Structural monitoring and integrity assessment of medieval towers. J. Struct. Eng. 132, 1681–1690. https://doi.org/10.1061/(asce)0733-9445(2006)132:11(1681).
Carpinteri, A., Lacidogna, G., 2007. Damage evaluation of three masonry towers by acoustic emission. Eng. Struct. 29, 1569–1579. https://doi.org/10.1016/j.engstruct.2006.08.008.
Carpinteri, A., Lacidogna, G., Niccolini, G., 2011. Damage analysis of reinforced concrete buildings by the acoustic emission technique. Struct. Control Health Monit. 18, 660–673. https://doi.org/10.1002/stc.393.
Carpinteri, A., Xu, J., Lacidogna, G., Manuello, A., 2012. Reliable onset time determination and source location of acoustic emissions in concrete structures. Cement Concr. Compos. 34 (4), 529–537. https://doi.org/10.1016/j.cemconcomp.2011.11.013.
Carpinteri, A., Lacidogna, G., Corrado, M., Di Battista, E., 2016. Cracking and crackling in concrete-like materials: a dynamic energy balance. Eng. Fract. Mech. 155, 130–144. https://doi.org/10.1016/j.engfracmech.2016.01.013.
Chen, Z., Zhang, G., He, R., Tian, Z., Fu, C., Jin, X., 2023. Acoustic emission analysis of crack type identification of corroded concrete columns under eccentric loading: a

comparative analysis of RA-AF method and Gaussian mixture model. Case Stud. Constr. Mater. 18, e02021. https://doi.org/10.1016/j.cscm.2023.e02021.
Colombo, S., Main, I., Forde, M., 2003. Assessing damage of reinforced concrete beam using "b-value" analysis of acoustic emission signals. J. Mater. Civ. Eng. 15, 280–286. https://doi.org/10.1061/(ASCE)0899-1561(2003)15:3(280).
De Larrard, F., Sedran, T., 1994. Optimization of ultra-high-performance concrete by the use of a packing model. Cement Concr. Res. 24 (6), 997–1009. https://doi.org/10.1016/0008-8846(94)90022-1.
Du, Y., Zang, Y., Li, X., Li, Y., Wen, W., Ruan, S., 2024. Assessing the influence of external curing on the early drying shrinkage of ultra-high-performance concrete. J. Build. Eng. 89, 109292. https://doi.org/10.1016/j.jobe.2024.109292.
Ge, M., 2003a. Analysis of source location algorithms, part I: overview and non-iterative methods. J. Acoust. Emiss. 21, 14–28.
Ge, M., 2003b. Analysis of source location algorithms, part II: iterative methods. J. Acoust. Emiss. 21, 29–51.
Guzmán, C., Torres, D., Hucailuk, C., Filipussi, D., 2015. Analysis of the acoustic emission in a reinforced concrete beam using a four points bending test. Procedia Mater. Sci. 8, 148–154. https://doi.org/10.1016/j.mspro.2015.04.058.
Han, Q., Yang, G., Xu, J., Fu, Z., Lacidogna, G., Carpinteri, A., 2019. Acoustic emission data analyses based on crumb rubber concrete beam bending tests. Eng. Fract. Mech. 210, 189–202. https://doi.org/10.1016/j.engfracmech.2018.05.016.
Huang, Z., Cuenca, E., Ferrara, L., 2024. Incorporation of self-healing of UHPC in structural design approaches through healable crack width threshold and kinetics: the case study of H2020 project ReSHEALience database. Dev. Built Environ. 18, 100388. https://doi.org/10.1016/j.dibe.2024.100388.
Jiang, Z., Zhu, Z., Accornero, F., Wang, C., 2024a. Multi-technique analysis of seawater impact on the performance of calcium sulphoaluminate cement mortar. Constr. Build. Mater. 443, 137717. https://doi.org/10.1016/j.conbuildmat.2024.137717.
Jiang, Z., Zhu, Z., Accornero, F., 2024b. Tensile-to-shear crack transition in the compression failure of steel-fibre-reinforced concrete: insights from acoustic emission monitoring. Buildings 14 (7), 2039. https://doi.org/10.3390/buildings14072039.
Kang, M., Kang, M.C., Yonis, A., Vashistha, P., Pyo, S., 2024. Effect of steel slag on the mechanical properties and self-sensing capability of ultra-high performance concrete (UHPC). Dev. Built Environ. 17, 100342. https://doi.org/10.1016/j.dibe.2024.100342.
Lacidogna, G., Piana, G., Accornero, F., Carpinteri, A., 2020. Multi-technique damage monitoring of concrete beams: acoustic emission, digital image correlation, dynamic identification. Constr. Build. Mater. 242, 118114. https://doi.org/10.1016/j.conbuildmat.2020.118114.
Li, C., Shi, Y., Zhou, J., Fang, C., He, J., He, L., 2023. Experimental investigation on UHPC shrinkage of full-scale steel-UHPC composite bridge deck. Dev. Built Environ. 16, 100281. https://doi.org/10.1016/j.dibe.2023.100281.
Liu, Y., Wei, Y., Ma, L., Wang, L., 2022. Restrained shrinkage behavior of internally-cured UHPC using calcined bauxite aggregate in the ring test and UHPC-concrete composite slab. Cement Concr. Compos. 134. https://doi.org/10.1016/j.cemconcomp.2022.104805.
Manuello, A., Niccolini, G., Carpinteri, A., 2019. AE monitoring of a concrete arch road tunnel: damage evolution and localization. Eng. Fract. Mech. 210, 279–287. https://doi.org/10.1016/j.engfracmech.2018.07.029.
Niccolini, G., Lacidogna, G., Carpinteri, A., 2019. Fracture precursors in a working girder crane: AE natural-time and b-value time series analyses. Eng. Fract. Mech. 210, 393–399. https://doi.org/10.1016/j.engfracmech.2018.05.029.
Ohtsu, M., 2015. Acoustic Emission and Related Non-destructive Evaluation Techniques in the Fracture Mechanics of Concrete Fundamentals and Applications. Elsevier.
Shiotani, T., Fujii, K., Aoki, T., Amou, K., 1994. Evaluation of progressive failure using AE sources and improved b-value on slope model tests. Prog. Acoust. Emiss. VII Jsndi 529–534.
Shiotani, T., Osawa, S., Momoki, S., Ohtsu, H., 2015. Visualization of damage in RC bridge deck for bullet trains with AE tomography. Adv. Acoust. Emiss. Technol. 158, 357–368.
Sobuz, H., Visintin, P., Ali, M., Singh, M., Griffith, M., Sheikh, A., 2016. Manufacturing ultra-high performance concrete utilising conventional materials and production methods. Constr. Build. Mater. 111, 251–261. https://doi.org/10.1016/j.conbuildmat.2016.02.102.
Soliman, A., Nehdi, M., 2014. Effects of shrinkage reducing admixture and wollastonite microfiber on early-age behavior of ultra-high performance concrete. Cement Concr. Compos. 46, 81–89. https://doi.org/10.1016/j.cemconcomp.2013.11.008.
Teng, L., Valipour, M., Khayat, K., 2021. Design and performance of low shrinkage UHPC for thin bonded bridge deck layer. Cement Concr. Compos. 118, 103953. https://doi.org/10.1016/j.cemconcomp.2021.103953.
Tutkun, B., Barlay, E., Yalçinkaya, Ç., Yazici, H., 2023. Effect of internal curing on shrinkage and cracking potential under autogenous and drying conditions. Constr. Build. Mater. 409. https://doi.org/10.1016/j.conbuildmat.2023.134078.
Valipour, M., Khayat, K., 2018. Coupled effect of shrinkage-mitigating admixtures and saturated lightweight sand on shrinkage of UHPC for overlay applications. Constr. Build. Mater. 184, 320–329. https://doi.org/10.1016/j.conbuildmat.2018.06.191.
Wang, C., Jiang, Z., Accornero, F., Zhou, S., Ou, Q., 2024. Influence of seawater and salt ions on the properties of calcium sulfoaluminate cement. J. Mater. Civ. Eng. 37 (6). https://doi.org/10.1061/JMCEE7.MTENG-19193.
Wang, D., Shi, C., Wu, Z., Xiao, J., Huang, Z., Fang, Z., 2015. A review on ultra high performance concrete: Part II. Hydration, microstructure and properties. Constr. Build. Mater. 96, 368–377. https://doi.org/10.1016/j.conbuildmat.2015.08.095.
Wu, L., Farzadnia, N., Shi, C., Zhang, Z., Wang, H., 2017. Autogenous shrinkage of high performance concrete: a review. Constr. Build. Mater. 149, 62–75. https://doi.org/10.1016/j.conbuildmat.2017.05.064.
Xie, T., Fang, C., Ali, M.S.M., Visintin, P., 2018. Characterizations of autogenous and drying shrinkage of ultra-high performance concrete (UHPC): an experimental study. Cement Concr. Compos. 91, 156–173. https://doi.org/10.1016/j.cemconcomp.2018.05.009.
Zheng, S., You, W., Wang, C., Liu, X., Khan, I., Yang, G., 2023. Shrinkage and cracking sensibility of steel-alkali activated UHPC composite bridge decks. Constr. Build. Mater. 385. https://doi.org/10.1016/j.conbuildmat.2023.131431.
Zhu, Z., Tao, Y., Xiang, Z., Huang, Y., Zhou, Y.E., Shao, X., 2018. Stress behaviors and fatigue performance of details in orthotropic steel bridges with UHPC-deck plate composite system under in-service traffic flows. J. Bridge Eng. 23 (3). https://doi.org/10.1061/(ASCE)BE.1943-5592.0001167, 04017142-1~21.
Zhu, Z., Zhu, R., Xiang, Z., 2023. A review on behavior and fatigue performance of orthotropic steel–UHPC composite deck. Buildings 13 (8), 1906. https://doi.org/10.3390/buildings13081906.
Zhu, Z., Jiang, Z., Accornero, F., Carpinteri, A., 2024. Correlation between seismic activity and acoustic emission on the basis of in-situ monitoring. Nat. Hazards Earth Syst. Sci. 24 (11), 4133–4143. https://doi.org/10.5194/nhess-24-4133-2024.
Zhu, Z., Jiang, Z., Accornero, F., 2025. Size-scale and time-scale effects on the failure of UHPC-strengthened reinforced concrete beams. Structures 78, 109248. https://doi.org/10.1016/j.istruc.2025.109248.